Master Géotechnique, Civil Engineering

Numerical modelling of monopile behavior under cyclic lateral loadings in sand

Marina Al Bacha

Submitted in fulfillment of the requirements for the degree of

Master in Civil Engineering

‶Géotechnique, Civil Engineering″

Lebanese University

September 2021

Project Advisors:

- Matthieu Blanc, UGE \ GERS – GC
- Semaan Maatouk, UGE \ GERS – GC

Examiner at Home University:

- Fadi Hage Chehade, Lebanese University

Acknowledgement

I would like to express my most vital and sincere thanks to Matthieu Blanc, director of the geotechnical centrifuges Laboratory, who nourished and guided my internship project to achieve the goal. I would like also to thank, Semaan Maatouk, supervisor of my project, who has invested his full effort in discussing with me the issues, and whose contribution in stimulating suggestions and encouragement, helped me to coordinate my project especially in writing.

A special gratitude to Professor Luc Thorel, who accepted me within the laboratory and providing me all the conditions so that I can carry out this internship in better conditions. I would particularly like to thank him for the interest he has brought to my work.

Furthermore, I would like to acknowledge with much appreciation the crucial role of Professor Abdul Hamid Soubra who helped me to find this internship project.

Last but not least, many thanks go to my parents and my family for instilling me with a strong passion for learning and for doing everything possible to put me on the path to greatness.

List of contents

Abstract

Offshore Wind Turbines (OWTs) are widespread in Europe for the purpose of producing clean energy. Monopiles are widely used as foundations for OWTs in shallow coastal water. Over their design service life, the monopiles are subjected to long-term cyclic lateral loading due to wind, current and waves, leading to an accumulation of displacement or rotation in the foundations. The worst scenario occurs when the accumulation of displacement never reaches a stable state: the so-called 'Ratcheting phenomenon'. The purpose of this internship is to explore the HARM (hyperplastic accelerated ratcheting model) model that allows to capture the 'Ratcheting' effect. Numerical simulations, therefore have been performed to predict the response of monopiles under cyclic loadings. Besides, centrifuged horizontal tests have been conducted on an impact-driven monopiles to calibrate the numerical model.

Résumé

Les éoliennes offshores sont répandues en Europe dans le but de produire de l'énergie propre. Dans les eaux côtières peu profondes, les monopieux sont largement utilisés à ce jour comme fondations pour les éoliennes offshores. Au cours de leur durée de service, ces monopieux sont soumis à des chargements cycliques latéraux à long terme dus aux vents, aux courants et aux vagues. Ce qui entraîne une accumulation de déplacement ou de rotation dans les fondations. Le pire scénario se produit lorsque l'accumulation de déplacement n'atteint jamais un état stable : c'est le 'phénomène de Ratcheting'. Le but de ce stage est d'explorer le modèle HARM (hyperplastic accelerated ratcheting model) qui permet de capturer l'effet de 'Ratcheting'. Des simulations numériques ont donc été réalisées pour prédire la réponse des monopieux sous chargements cycliques. En outre, des essais horizontaux centrifugés ont été effectués sur un monopieu installé par battage afin de calibrer le modèle numérique.

Notations

Latinas uppercases

D	Monopile diameter (L)
E	Initial tangent shear modulus (-)
G	Monopile shear modulus (FL^{-2})
H	Lateral force on top of the pile (F)
H_{n}, $\hat{H}$	Kinematic hardening modulus (FL^{-2})
H_{R}	Ultimate force for normalization (F)
H_{max}	Maximum applied lateral force on top of the pile (F)
H_{min}	Minimum applied lateral force on top of the pile (F)
L	Monopile embedment length (L)
M	Moment applied at the base of monopile (FL^{-1})
N	Number of cycles (-)
N_{g}	g level (-)
N_{s}	Number of kinematic hardening surfaces (-)
R_0	Initial ratcheting rate (-)
R_{beta}	Ratcheting rate (-)
$\hat{R}$, R_{n}	Ratcheting parameter (-)
$\mathrm{R}_{\mathrm{fac}}$	Accelerated factor (-)
$S(\sigma)$	Modified/generalised signum function $\begin{cases} S(\sigma)=1 & x>0 \\ S(\sigma)=-1 & x<0 \\ S(\sigma)\in[-1,1] & x=0 \end{cases}$

Latinas lowercases

d	Dissipation potential (-)
f	Specific Helmholtz free energy (FL^{-2})
k_{n}, $\hat{k}$	Kinematic hardening surface strengths (FL^{-2})
k_{U}	Upper limit stress (FL^{-2})
l_{e}	Load eccentricity (L)
m_{h}	Monotonic exponent defining shape of initial loading curve (-)
m_{k}	Exponent defining rate at which the hysteresis loop closes with hardening parameter (-)
m_{r}	Exponent defining dependence of rate of ratcheting on hardening parameter (-)
m_{s}	Exponent defining dependence of rate of ratcheting on stress (-)
m_{α}	Empirical exponent defining evolution of accumulated rotation with cycle number (-)
t	Monopile wall thickness (L)

Greeks

α, α_{n}, $\hat{\alpha}$	Internal kinematic variable (-)
α_{r}	Ratcheting strain (-)
$\dot{\alpha}_{\mathrm{r}}$	Rate of ratcheting strain (-)
β	Accumulation of ratcheting strain (-)
β_0	Initial value of hardening parameter (-)
ε	Total strain (-)
ε^{e}	Elastic strain (-)

$\varepsilon_{\mathrm{pu}}$	Ultimate monotonic plastic strain defining shape of loading curve (-)
η	Internal coordinate (-)
ν_{T}	Lateral displacement at the head of the pile (L)
ν_{TR}	Ultimate displacement for normalization (L)
θ_{G}	Rotation of monopile neutral axis at ground level (°)
ρ_{dmax}	maximum dry density (FL^{-3})
ρ_{dmin}	minimum dry density (FL^{-3})
ρ_{s}	dry density of solid particles (FL^{-3})
σ	Applied normalized stress (-)
σ_0	Initial applied stress (-)

List of figures

List of tables

1 Introduction

Global warning and the challenges of the development of renewable energies have stimulated the onshore wind energy sector, but especially the offshore sector. The development of offshore wind has progressed rapidly in Europe. Figure 1 illustrates the growth of this sector over the last years.

The offshore wind turbines (OWTs) are based on the same principles as onshore wind turbines. Though, they benefit from more several advantages: the wind is more regular at sea and stronger, which makes it possible to install turbines of greater power operating more often and more regularly. Furthermore, since these turbines have no impact on the environment, larger wind turbine can be installed.

The OWTs are designed to withstand severe environmental loads. Over their design service life, typically 20-25 years, these complex systems are subjected to significant high-cyclic lateral loadings and overturning moments due to wind, waves, blades rotation or even seismic origin. Such cyclic loads are varying in amplitude, direction and frequency. They are transmitted to the ground as cyclic stresses through the foundation, resulting in an accumulation of permanent deformations in the foundation. Therefore, the design of the support structure holding the turbines is a key concern.

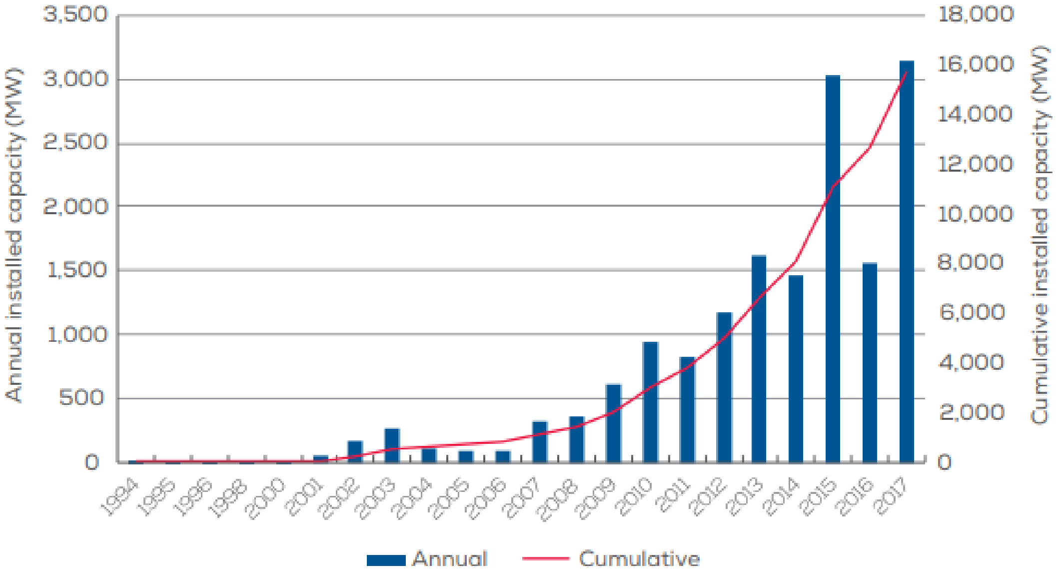

Figure 1: Cumulative and annual offshore wind energy installation (WindEurope, 2021)

1.1 The use of monopiles

The (OWTs) can be founded on different foundation types. Figure 2 illustrates a range of foundation that can be used for anchoring wind turbines (gravity base, jacket, monopile, etc…). The choice of these supports depends mainly on soil conditions, turbine size and water depth. Today monopiles are widely used in offshore wind farms in shallow water depths (Dupla et al., 2019) and represent 80% of OWT foundations installed in Europe (WindEurope, 2021). These monopiles are single open-ended steel tubes often embedded into the soil using a dynamic method: the so-called impact driving. Comparing to other foundations types, monopile foundations are less expensive, simple to design and simple to install.

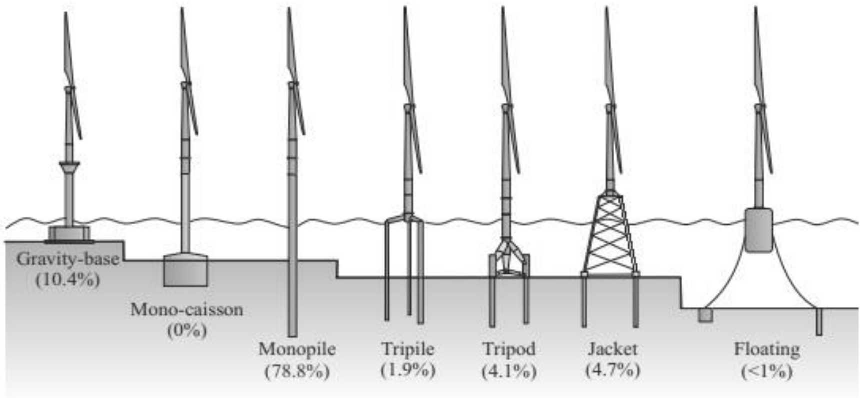

Figure 2: Different foundation types for offshore wind turbines (Abadie, 2015).

Monopiles have an outer diameter (D) ranging up to 8 m (Sørensen et al., 2017) with an embedment length-to-diameter ratio (L/D) between 3 and 6 (Schroeder et al., 2015; Sørensen et al., 2017). Future design tends to increase diameters to 10 m for the next generation in order to hold larger turbines in deeper water. These offshore turbine monopiles considered as rigid piles, are subjected to long-term displacements and rotations that could reduce the life time of the OWTs if the rotation exceeds a threshold of about 0.5° (Staubach and Wichtmann, 2020). The different loads acting on the monopiles are shown in Figure 3.

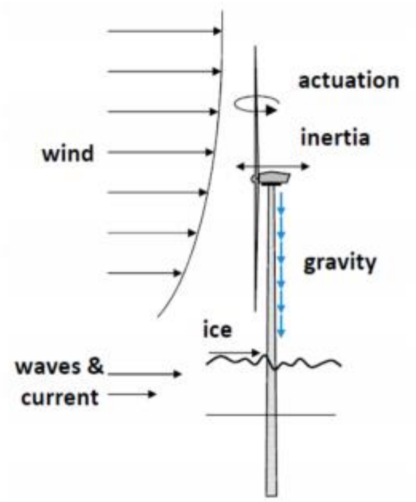

Figure 3: Loads acting on an offshore wind turbine (Beuckelaers, 2017).

1.2 Current foundation numerical modelling

Three existing design approaches can be considered to predict the monopile response to lateral loadings. These different models (described below and summarized in Figure 4) account for the pile-soil interaction that is a key concern in the most geotechnical engineering practice.

1) Three-dimensional Finite Element Analysis (3D FEA): it allows to capture the entire soil behavior and the interaction with the structure. It provides the most accurate and realistic response of the foundation. The model calibration is based on soil parameters from soil element testing and/or in-situ testing. This model is flexible for complex foundation geometries and complex soil layering. However, it is not appropriate to model monopiles when subjected to cyclic loadings, it cannot perform the response of the system cycle by cycle.

2) Winkler Foundation (known as p-y method in (Winkler, 1867)): this model represents the foundation as a beam and the soil-pile interaction is defined by a series of springs acting independently along the depth of the foundation. The calibration is based on empirical data or from 3D FE modelling. This Winkler approach can capture precisely the response for slender piles. However, a generalized form of the Winkler approach is achieved in the last few years by the joint industry project PISA (Byrne et al., 2020; Byrne et al., 2017) to capture the response of rigid piles under monotonic loading.

3) Macro-element: this model is an alternative to the Winkler approach so that the entire response of the pile is captured by springs at the soil surface. The macro-element approach is computationally fast, simple to proceed and allows to predict the global foundation response. This procedure is based on the hyperplasticity framework defined as HARM model (hyperplastic accelerated ratcheting model). The detailed approach is described in the following part.

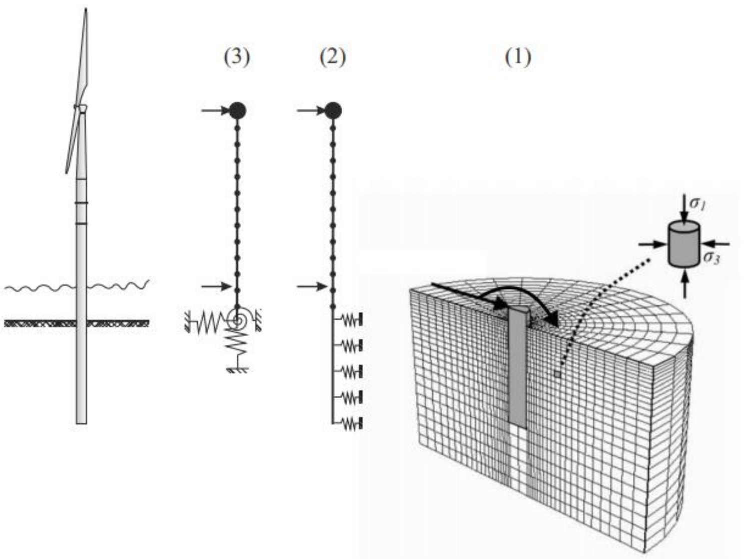

Figure 4: Schematic representation of the possible pile design methodologies (3D-FE mesh from Achmus et al., 2009).

1.3 Research objectives

In order to predict the response of monopiles under cyclic lateral loadings, this research is based on a macro-modelling of the monopile using the constitutive model (HARM). The HARM model founded on the hyperplasticity framework presented by Houlsby and Puzrin, (2006) allows to detect the ratcheting phenomenon (accumulation of irreversible deformation with cycle number). The model performance is established using numerical simulations and is fitted with experimental results. The experiments are conducted on a centrifuged monopile model impact-driven into a saturated dense sand. The calibration method used is proposed by Abadie et al., (2019).

2 Literature review

2.1 Outline of the Hyperplasticity approach

The hyperplastic model is initially presented by (Ziegler, 1977) and covered in details by Houlsby and Puzrin, (2006). This approach allows for modelling the non-linear behavior (plasticity models) of a dissipative material while conforming to Masing rule (Masing, 1926). The framework is applicable for many engineering materials, specifically in the area of geotechnical engineering.

Based on thermomechanical principles, the constitutive behavior of a dissipative material is defined by two scalar potential functions: the Gibbs free energy or the Helmholtz energy f presenting the energy stored in the system, and the dissipation function d defining the rate of energy dissipation. Both functions are able to capture the behavior of a material when it acts in a non-linear manner. The hyperplasticity framework will be enlarged in the interest of capturing the HARM model.

The response of a material can be described in different spaces: stress-strain space (σ,ε), lateral distributed load-displacement space (p,υ), distributed moment-rotation space (m,ψ), base horizontal force-displacement space (H_{B}, υ_{B}) or base moment-rotation (M_{B},ψ_{B}).

Starting from the potential functions f and d, the following section will present the mathematical configuration to reach the constitutive behavior of a dissipative material defined in the stress-strain space. An advantage of this model is that it can be used as a macro-element to represent the global monopile response.

The hyperplasticity framework is also appropriate to model shallow foundations (Houlsby et al., 2005) and suction caissons (Byrne et al., 2000).

2.2 Hierarchy of kinematic plasticity models

The elaboration of the constitutive HARM model starts with a hierarchy of plastic models that captures pure kinematic hardening behavior. The first model employs a single kinematically hardening yield surface, and it will be extended to multiple surfaces to produce smoother transitions from elastic to plastic behavior. However, these models will be generalized to infinite number of yield surfaces.

2.2.1 Single yield surface

The original model is the simplest plastic model, initially proposed by Prager, (1955) with linear hardening (linear elastic – perfectly plastic in 1D of loading). This model can be extended to an elasto-plastic model with single yield surface as presented in Figure 5(a). It is defined by a single yield surface composed of a spring with an elastic coefficient E in series with a slider with ultimate capacity k. The linear hardening is introduced by adding another spring with elastic modulus H in parallel with the sliding element.

Before the stress σ reaches the slip stress k of the slider, the system behaves linear elastic and the total displacement ε^{e} is ensured only by the elastic spring E as shown in Figure 5(b). Once the stress σ reaches the threshold k, the slider moves and the total response is now governed by both springs. An additional plastic strain α will be added to the elastic strain ε^{e}, resulting from the activation of the yield surface. The behavior is elasto-plastic with a linear hardening characterized by the tangent modulus E_1.

During the unloading phase, the stress σ started to decrease gradually and the behavior is linear elastic with the elastic coefficient E. When the stress reaches the opposite value of the slip stress $-k$, the behaviour returns to elasto-plastic with the tangent modulus E_1. When both springs will be activated, the energy f stored in the system is thus the sum of energies from both springs and the rate of dissipation of energy d will be the energy dissipated by the slider. The two energy functions are expressed as:

$$f(\varepsilon, \alpha) = \frac{E}{2}(\varepsilon - \alpha)^2 + \frac{H}{2}\alpha^2 \tag{1}$$

$$d = k|\dot{\alpha}| \tag{2}$$

Following the approach described in Puzrin and Houlsby, (2001), the mathematical development of both functions leads to the total incremental response ε:

$$\varepsilon = \varepsilon^e + \alpha = \frac{\sigma}{E} + \frac{\sigma - k}{H} \tag{3}$$

The tangent modulus E_1 can be found from Equation (3):

$$E_1 = \frac{d\sigma}{d\varepsilon} = \frac{EH}{E + H} \tag{4}$$

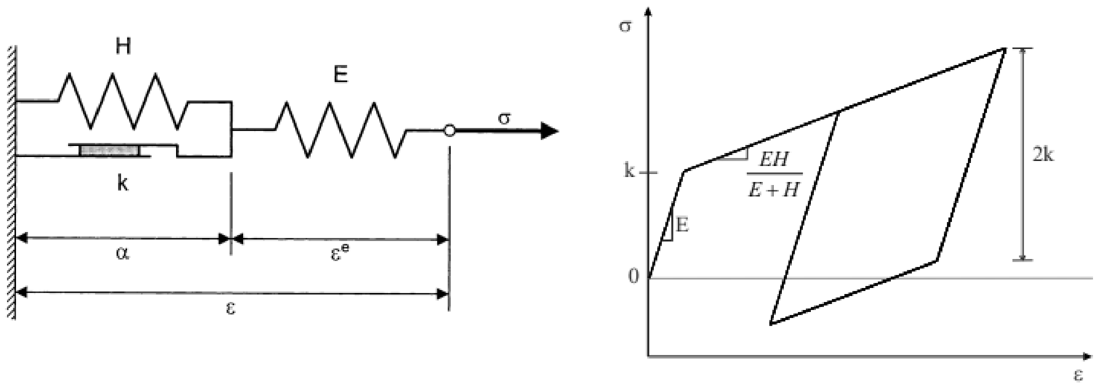

(a) (b)

Figure 5: (a) Schematic layout of Prager, 1955 [18] and (b) Typical response for single yield surface for kinematic hardening (Abadie, 2015).

2.2.2 Multiple yield surfaces

The model with a single yield surface can be generalized to multiple kinematic surfaces N_S, necessary to simulate a smooth elastic-plastic transition. These surfaces can be placed either in series (so-called series model) or in parallel (so-called parallel model) with an elastic spring E.

2.2.2.1 Series model

The series model is defined by springs with hardening modulus H_n placed in parallel with sliders with ultimate capacities k_n as shown in Figure 6. These surfaces are placed in series with an elastic spring E.

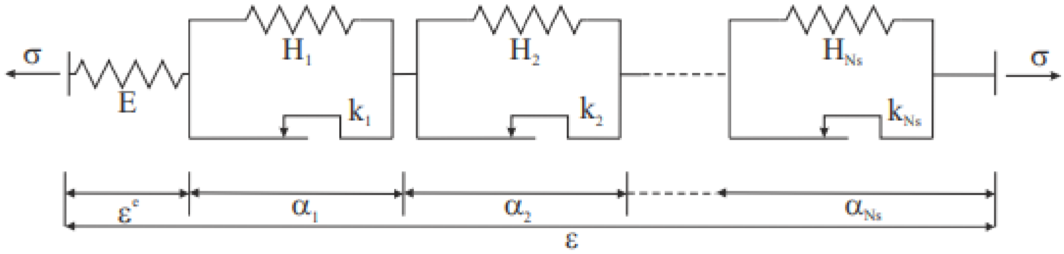

Figure 6: Schematic representation of multi-surface kinematic hardening model (Abadie, 2015).

When the stress σ started to exceed the ultimate strengths of sliders progressively, these sliders get into action. Hence, each spring-slider unit will provide pure kinematic hardening, resulting in a multi-linear stress-strain response (Figure 7(a)). For a large number of yield surfaces, the response becomes smoother (Figure 7(b)).

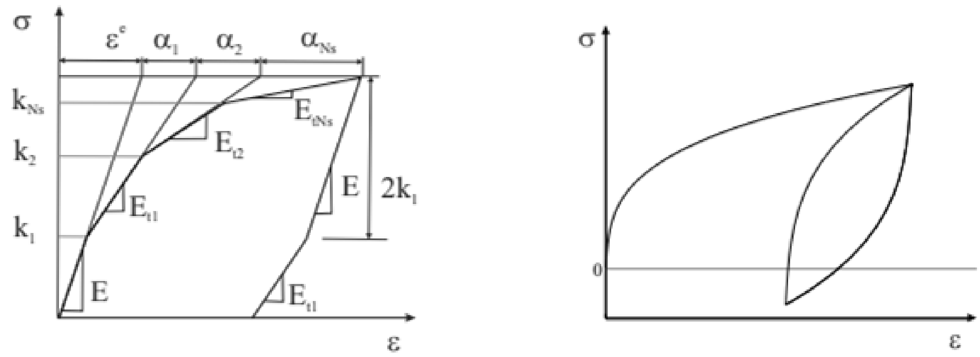

(a) (b)

Figure 7: Schematic representation (a) Response obtained with 3 kinematic hardening surfaces (Puzrin and Houlsby, 2001 [4]) and (b) Typical smooth response for large number of yield surfaces (Abadie, 2015).

The energy and flow potentials are now the sum of the individual contribution from each surface:

$$f = \frac{E}{2}\left(\varepsilon - \sum_{n=1}^{Ns} \alpha_{\mathrm{n}}\right)^2 + \sum_{n=1}^{Ns} \frac{H_{\mathrm{n}}}{2} \alpha_{\mathrm{n}}^2 \tag{5}$$

$$d = \sum_{n=1}^{Ns} k_{\mathrm{n}} |\dot{\alpha}_{\mathrm{n}}| \tag{6}$$

Where N_{s} is the number of yield surfaces and $\alpha_1, \alpha_2, \ldots., \alpha_{\mathrm{Ns}}$ are the plastic strains produced by each surface.

The same procedure used in Puzrin and Houlsby, (2001) for the single yield surface is used to calculate the incremental response for multiple yield surfaces:

$$\varepsilon = \varepsilon^{\mathrm{e}} + \sum_{n=1}^{Ns} \alpha_{\mathrm{n}} = \frac{\sigma}{E} + \sum_{n=1}^{Ns} \frac{\sigma - k_{\mathrm{n}}}{H_{\mathrm{n}}} \tag{7}$$

Where σ/E is the elastic response of the elastic spring E, and $\sum_{n=1}^{Ns} \alpha_{\mathrm{n}}$ is the sum of plastic strains resulting from the activation of yield surfaces.

Also, the tangent modulus E_{n} can be deduced from Equation (7):

$$E_{\mathrm{n}} = \frac{d\sigma}{d\varepsilon} = \frac{1}{\frac{1}{E} + \sum_{n=1}^{Ns} \frac{1}{H_{\mathrm{n}}}} \tag{8}$$

2.2.2.2 Parallel model

An equivalent model can be developed where the spring/slider elements act in parallel, as illustrated in Figure 8 for multi surface kinematic hardening. The model is also framed within the hyperplasticity but with different mathematical framework, and it conforms to Masing rule for the unload reload behavior. The mathematical formulation of the parallel model is detailed in Houlsby et al., (2017).

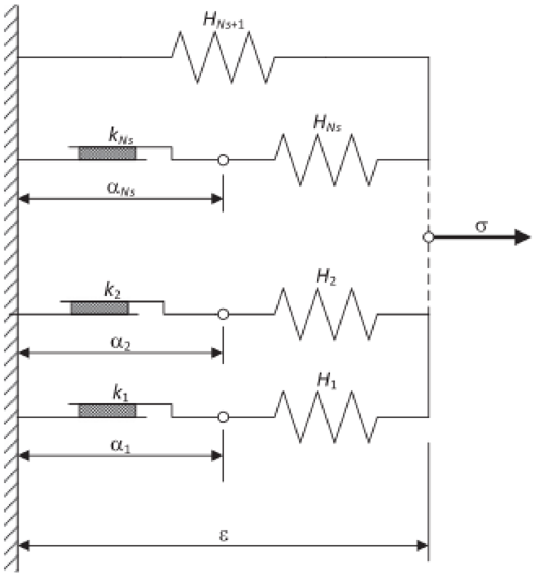

Figure 8: Multiple surface kinematic hardening plasticity (parallel form) (Houlsby et al., 2017).

As comparison between both models, stresses will become additive in the parallel form instead of the plastic strains as previously covered in the series model. As suggested by (Beuckelaers et al., 2018) the series model is considered for stress-controlled tests, while the parallel model become suitable for strain-controlled tests. In addition, (Beuckelaers et al., 2018) demonstrated that, for one-directional loading, the series and parallel models give identical response for pure kinematic hardening.

2.2.3 Infinite number of yield surfaces (continuous kinematic hardening hyperplasticity)

The discrete energy form can be extended to a continuous field for an infinite number of yield surfaces. The internal variables $\alpha_1, \alpha_2, \ldots \alpha_{\mathrm{Ns}}$, are now replaced by an internal function $\hat{\alpha}(\eta)$ and the Helmholtz free energy f and the flow potential d are expressed in an integral form instead of a discrete summation of a large number of yield surfaces as detailed in Abadie et al., (2019).

2.3 Masing rule

The Masing rule (Masing, 1926) is sustained when the HARM model is purely kinematic hardening, while the system is subjected to symmetric loading. The extension to ratcheting model allows also to obey approximately to Masing rule. The rule is verified by the following two conditions:

1) The unloading and reloading curves have the same slope as the initial loading curve (the hardening modulus H_n remain the same),
2) The ultimate capacities k_n of the initial loading (backbone curve) are multiplied by 2 in the unloading and reloading curves.

Masing rule had a powerful feature: it allows to deduce the hysteresis response (unload – reload) from the backbone curve equation.

Abadie, (2015) tends to check the Masing rule using experimental laboratory test at 1xg. The response of the symmetric reversed test, so-called H0, performed with one cycle is shown in Figure 9. The red curve in Figure 9(a) represents the initial loading curve deduced from the unloading curve (green curve) scaled down by 2 and plotted from the origin. This curve is approximately close to the backbone curve resulted from the experimental test.

In Figure 9(b), the reload curve (red curve) is obtained by mirror of the unload curve, which shows a good approximation with the test. Hence, both curves identify approximately Masing rule with some differences assigned to experimental errors.

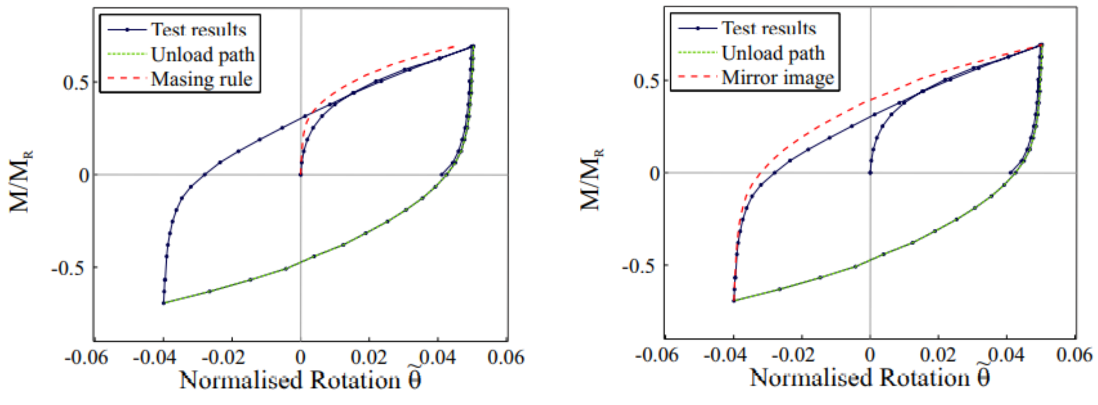

Figure 9: Test H0, application of Masing rules: (a) comparison of unloading path with initial loading curve (b) comparison of unloading path with reloading curve (Abadie, 2015).

2.4 Hyperplastic Accelerated Ratcheting Model (HARM) (series form)

2.4.1 Conceptual framework

The HARM Model used in Abadie et al., (2019) is framed within the multi surface plasticity model using the pure kinematic hardening formulated based on the series model. The generalization of this model enables to capture the ratcheting phenomenon detected after a large number of cycles while conforming approximately to Masing Rule. Another powerful feature of HARM model is that it can accelerate the effects of cyclic loadings.

The effect of ratcheting is considered by adding another slider that accounts for an additional plastic strain defined as α_r (Figure 10(a)). The ratcheting element gets into action each time that at least one of the yield surfaces is active. Each surface is characterized by a ratcheting parameter R_{n}.

During unloading-reloading the material, hysteretic behavior occurs resulting from the accumulation of plastic strains from a cycle to another (Figure 10(b)). Note that the hysteresis loop closes when the ratcheting is disabled (Figure 11), also called plastic accommodation.

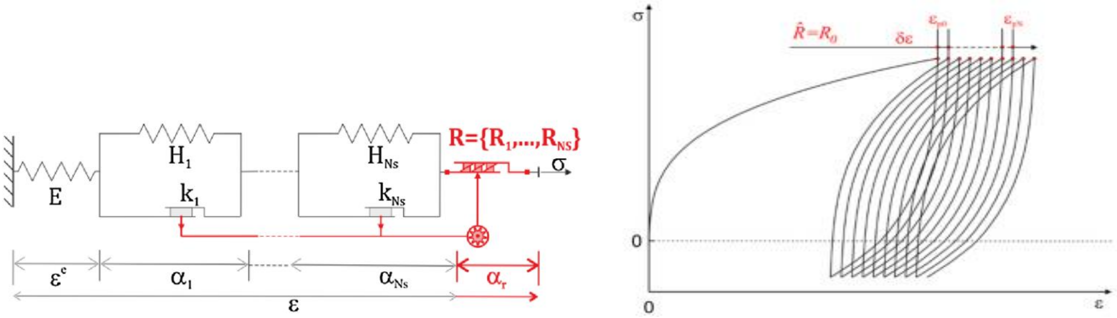

(a) (b)

Figure 10: (a) Schematic representation and (b) Typical response continuous cyclic loading obtained with HARM (Abadie et al., 2019).

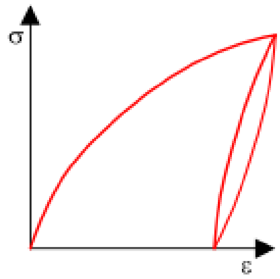

Figure 11: Closed hysteresis loop on unloading (Houlsby et al., 2017).

2.4.2 Mathematical formulation in discrete form

For multiple yield surfaces, the series model is defined through the two potential functions f and d (Equation (9) and Equation (10) respectively). The derivation within the plasticity framework leads to the incremental behavior expressed in terms of plastic strains and additional ratcheting strain (Equation (11) and Equation (12) respectively).

$$f = \frac{E}{2}\left(\varepsilon - \sum_{n=1}^{Ns} \alpha_{\mathrm{n}} - \alpha_{\mathrm{r}}\right)^2 + \sum_{n=1}^{Ns} \frac{H_{\mathrm{n}}}{2} \alpha_{\mathrm{n}}^2 \tag{9}$$

$$d = \sum_{n=1}^{Ns} k_{\mathrm{n}} |\dot{\alpha}_{\mathrm{n}}| + |\sigma||\dot{\alpha}_{\mathrm{r}}| \tag{10}$$

$$d\varepsilon = \frac{d\sigma}{E} + \sum_{n=1}^{Ns} d\alpha_{\mathrm{n}} + d\alpha_{\mathrm{r}} \tag{11}$$

$$d\alpha_{\mathrm{r}} = S(\sigma)\sum_{n=1}^{Ns} R_{\mathrm{n}}|d\alpha_{\mathrm{n}}| \tag{12}$$

For marge cycle number, the computation of the constitutive model becomes time consuming when modelling every single cycle incrementally. Therefore, the HARM model offers a powerful aspect that accelerates the effect of ratcheting with the same response when modelling with the incremental method. This is achieved by multiplying the initial ratcheting rate R_0 by a new factor R_{fac} that accelerates the model by skipping the number of cycles having the same amplitude. Therefore Equation (12) can be written as follows:

$$d\alpha_{\mathrm{r}} = R_{\mathrm{fac}}.\left(S(\sigma).\sum_{n=1}^{Ns} R_{\mathrm{n}}|\dot{\alpha}_{\mathrm{n}}|\right) \tag{13}$$

2.4.3 Mathematical formulation in integral form

When considering an infinite number of yield surfaces, the above discrete equations are also expressed in integral form:

$$f = \frac{E}{2}\left(\varepsilon - \int_0^{Ns} \hat{\alpha}\, d\eta - \alpha_{\mathrm{r}}\right)^2 + \int_0^{Ns} \frac{\widehat{H}}{2}\hat{\alpha}^2 d\eta \tag{14}$$

$$d = \int_0^{Ns} \hat{k}|\dot{\hat{\alpha}}|d\eta + |\sigma||\dot{\alpha}_{\mathrm{r}}| \tag{15}$$

$$d\varepsilon = \frac{d\sigma}{E} + \int_0^{Ns} d\alpha d\eta + d\alpha_{\mathrm{r}} \tag{16}$$

$$d\alpha_{\mathrm{r}} = S(\sigma)\int_0^{Ns} \hat{R}|d\hat{\alpha}|d\eta \tag{17}$$

$$d\beta = |d\alpha_{\mathrm{r}}| \tag{18}$$

Where the ratcheting rate $\hat{R}$ developed in Abadie et al., (2019) is expressed as:

$$\hat{R} = R_0\left(\frac{\hat{k}(\eta)}{k_{\mathrm{U}}}\right)\left(\frac{\beta}{\beta_0}\right)^{-m_{\mathrm{r}}}\left(\frac{|\sigma|}{\sigma_0}\right)^{m_{\mathrm{s}}} \tag{19}$$

R_0 is the initial ratcheting rate, β_0 the initial ratcheting strain and σ_0 the initial applied stress. This particular form of ratcheting rate is obtained by taking into consideration three aspects:

1) Decreased ratcheting rate with cyclic history: this aspect is achieved by expressing the ratcheting rate as $R_0\left({}^{\beta}/_{\beta_0}\right)^{-m_r}$, where $\hat{R}$ is decaying with β using a power law, and m_{r} is an exponent that defines the dependence of rate of ratcheting on hardening parameter (if $m_{\mathrm{r}} = 0$, the rate of ratcheting remains constant (Figure 10(b)),

2) Increased ratcheting rate with load intensity, by the implementation of the term $\left({|\sigma|}/{\sigma_0}\right)^{m_s}$, where $m_s(> 1)$ defines the dependence of the ratcheting rate on the stress,
3) Independent rate within surfaces, the ratcheting rate depends on the ultimate strength of each surface using the term $\left({\hat{k}(\eta)}/{k_U}\right)$, the ratcheting rate is proportional to the surface strengths,

Figure 13 emphasizes two main features for the ratcheting behavior:

1) Decreasing of ratcheting rate with cycle number and its dependency on the cycle magnitude,
2) Tightening of the hysteresis loop progressively which allows for increasing the stiffness.

2.5 Macro-modelling approach of the HARM model

2.5.1 Overview

The macro-element model to simulate the response of an offshore wind turbine foundation is illustrated in Figure 12. Lateral loads resulting from wind and waves are reduced to a horizontal lateral force and an overturning moment applied at the ground-level of the monopile. This set of loads are equivalent to a lateral load H applied at the head of the monopile with an eccentricity $l_e = M/H$ from the ground level. The coupled torsional M-θ and horizontal H-ν_G reactions at the ground surface level are therefore replaced by a unique horizontal reaction H-ν_T at the head of the monopile to simplify the problem. In this manner, the approach studied is a 0-D macro-element model at the ground surface.

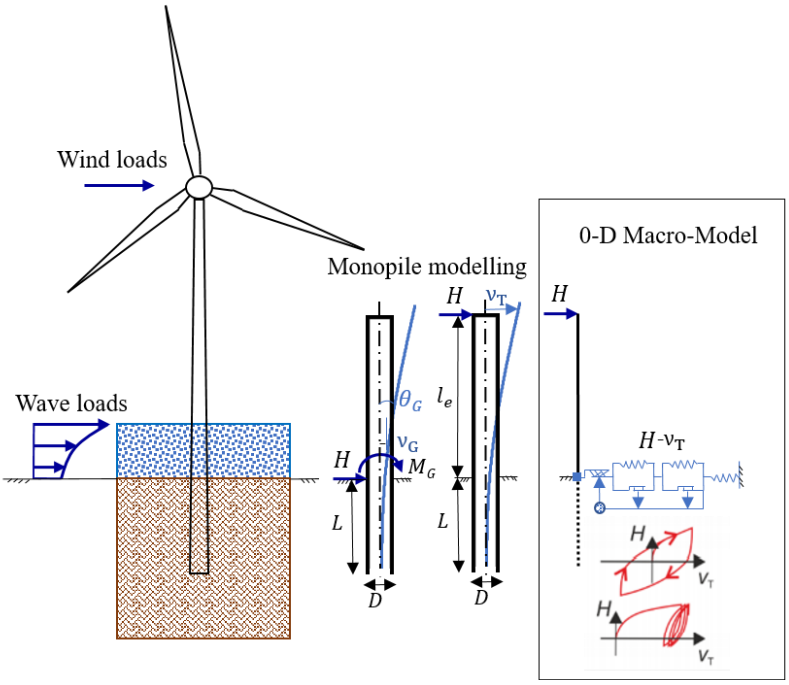

Figure 12: Schematic representation of monopile O-D macro-modelling

The monopile response is expressed in the stress-strain space after normalization of the lateral force H and the lateral displacement ν_T at the head of the monopile, with respect to reference values at ultimate capacity (H_R and ν_{TR} respectively) (Abadie et al., 2019). The values of H_R and ν_{TR} are obtained from the monopile response derived from experiments (discussed later).

$$\sigma = \frac{H}{H_R} \tag{20}$$

$$\varepsilon = \frac{\nu_T}{\nu_{TR}} \tag{21}$$

The ultimate stress can then be deduced:

$$\sigma_p = \sigma_{max} = \frac{H_{max}}{H_R} \tag{22}$$

Where H_{max} is the maximum applied lateral load.

2.5.2 Schematic representation of the monopile response

The monopile response under cyclic lateral loading, without (black curve) and with (blue curve) consideration of the ratcheting effects, are presented in Figure 13. The initial loading-unloading cycle is indexed '0' to indicate that this loop relates to the backbone curve. Subsequent loops are characterized by their number of cycles and load amplitude. The load amplitude is defined by the maximum and minimum normalized loads denoted by σ_p and σ_m respectively, where p_N and m_N are the peak (maximum) and minimum cycle points at the cycle number N.

At the peak point p_0, Equation (16) can be expressed as:

$$\varepsilon_{p0} = \frac{\sigma_p}{E} + \int_0^{p_0} d\hat{\alpha}(\eta) + (\beta_{p0} - \beta_0) \tag{23}$$

Where σ_p/E is the elastic strain, $\int_0^{p_0} d\hat{\alpha}(\eta)$ is the accumulated plastic strain, β_{p0} is the ratcheting deformation at the maximum initial point p_0 and β_0 is a small arbitrary value of ratcheting strain. $(\beta_{pN} - \beta_{p0})$ is the accumulated ratcheting strain in the cycle 'N' during cyclic loading.

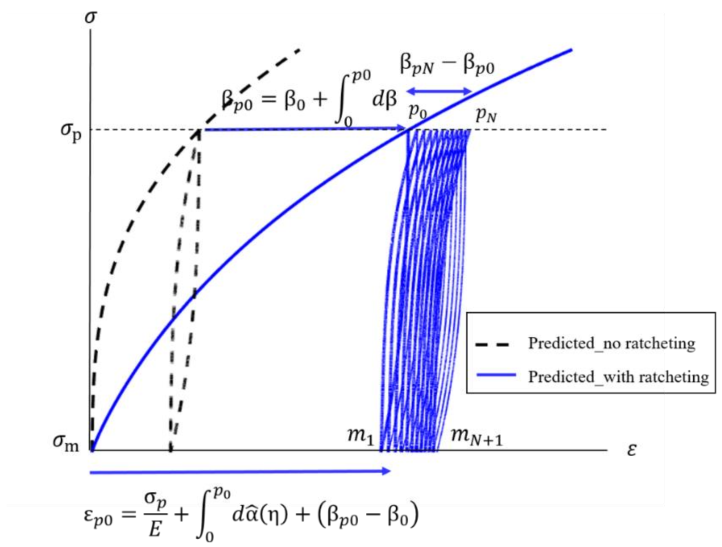

Figure 13: Monopile response and notations.

2.5.3 Formulation of the macro-element modelling

2.5.3.1 Initial loading response without ratcheting

During the initial loading phase, when the ratcheting is disabled $\hat{R} = 0$, the pure kinematic response of the backbone curve is obtained as follow by integrating Equation (16).

$$\hat{\alpha} = \frac{\sigma - \hat{k}}{\hat{H}} = \left(\sigma - k_{\mathrm{U}} \frac{\eta}{N_{\mathrm{s}}}\right) \frac{m_{\mathrm{h}}(m_{\mathrm{h}} - 1)}{N_{\mathrm{s}}} \frac{\varepsilon_{\mathrm{pu}}}{k_{\mathrm{U}}} \left(\frac{\eta}{N_{\mathrm{s}}}\right)^{m_{\mathrm{h}}-2}, \eta \in \left[0, \frac{\sigma}{k_{\mathrm{U}}} N_{\mathrm{s}}\right] \tag{24}$$

Where k_{U} is the ultimate strength of the sliders, $\varepsilon_{\mathrm{pu}}$ is the ultimate plastic strain and m_h is an exponent that defines the shape of the backbone curve.

2.5.3.2 Consideration of the ratcheting effect on the initial loading

The additional plastic strain β due to ratcheting effect for initial loading is obtained by integrating Equation (17) and replacing the ratcheting rate by its particular form as described before in Equation (19). The procedure leads to an increasing β function as follow:

$$\left(\frac{\beta}{\beta_0}\right)^{m_r+1} = 1 + \frac{\varepsilon_{\mathrm{pu}} R_0}{\beta_0} \frac{(m_{\mathrm{h}} - 1)(m_{\mathrm{r}} + 1)}{m_{\mathrm{s}} + m_{\mathrm{h}} + 1} \left(\frac{\sigma}{k_{\mathrm{U}}}\right)^{m_{\mathrm{s}}+m_{\mathrm{h}}+1} \tag{25}$$

At peak point load $\sigma = \sigma_{\mathrm{p}}$,

$$\left(\frac{\beta_{\mathrm{p}}}{\beta_0}\right)^{m_{\mathrm{r}}+1} = 1 + \frac{\varepsilon_{\mathrm{pu}} R_0}{\beta_0} \frac{(m_{\mathrm{h}} - 1)(m_{\mathrm{r}} + 1)}{m_{\mathrm{s}} + m_{\mathrm{h}} + 1} \left(\frac{\sigma_{\mathrm{p}}}{k_{\mathrm{U}}}\right)^{m_{\mathrm{s}}+m_{\mathrm{h}}+1} \tag{26}$$

2.5.3.3 Unloading-loading response for each cycle

The plastic strains of unloading-reloading curves are deduced from Equation (24) of the backbone, by scaling the strengths of the sliders by a factor of 2 (based on the Masing rule). The ratcheting strains of both curves can be obtained following the same procedure of the backbone curve also by conforming to Masing rule.

For unloading and loading the monopile, the accumulation of plastic strain due to ratcheting is expressed, in Equation (27) and Equation (28) respectively as follow:

$$\beta_{\mathrm{m}}^{m_{\mathrm{r}}+1} = \beta_{\mathrm{p}}^{m_{\mathrm{r}}+1} + \beta_0^{m_{\mathrm{r}}} \frac{(m_{\mathrm{h}} - 1)(m_{\mathrm{r}} + 1)\varepsilon_{\mathrm{pu}} R_0}{2^{m_{\mathrm{h}}}} \left(\frac{\sigma_{\mathrm{p}}}{k_{\mathrm{U}}}\right)^{m_{\mathrm{s}}+m_{\mathrm{h}}+1} \int_x^1 (1-t)^{m_{\mathrm{h}}} dt \tag{27}$$

$$\beta_{\mathrm{p}}^{m_{\mathrm{r}}+1} = \beta_{\mathrm{m}}^{m_{\mathrm{r}}+1} + \beta_0^{m_{\mathrm{r}}} \frac{(m_{\mathrm{h}} - 1)(m_{\mathrm{r}} + 1)\varepsilon_{\mathrm{pu}} R_0}{2^{m_{\mathrm{h}}}} \left(\frac{\sigma_{\mathrm{p}}}{k_{\mathrm{U}}}\right)^{m_{\mathrm{s}}+m_{\mathrm{h}}+1} \int_1^x (1-t)^{m_{\mathrm{h}}} dt \tag{28}$$

Where $\int_1^x (1-t)^{m_{\mathrm{h}}} dt$ is the incomplete beta function.

2.5.3.4 Accumulation of ratcheting with cycle number

The accumulation of the ratcheting strain with cyclic loadings is obtained using recurrence procedure of subsequent loops (Equation (27) and Equation (28) for unloading and reloading curves respectively). Note that the method is detailed in Abadie et al., (2019).

$$\beta_{\mathrm{pN}}^{m_{\mathrm{r}}+1} = \beta_{\mathrm{p0}}^{m_{\mathrm{r}}+1} + N \frac{\beta_0^{m_{\mathrm{r}}} R_0 (m_{\mathrm{h}} - 1)(m_{\mathrm{r}} + 1)\varepsilon_{\mathrm{pu}}}{2^{m_{\mathrm{h}}}} \left(\frac{\sigma_{\mathrm{p}}}{k_{\mathrm{U}}}\right)^{m_{\mathrm{s}}+m_{\mathrm{h}}+1} \left(B(m_{\mathrm{s}} + 1, m_{\mathrm{h}} + 1) + \frac{1}{m_{\mathrm{s}} + m_{\mathrm{h}} + 1}\right) \tag{29}$$

Where $B(m_{\mathrm{s}} + 1, m_{\mathrm{h}} + 1)$ is the beta function.

Equation (29) shows that $\beta_{\mathrm{pN}}^{\mathrm{m_r}+1}$ accumulates linearly with the number of cycles N. For simplification, the ratcheting strain β_{pN} can be approximated also by a power law (Abadie et al., 2019):

$$\beta_{\mathrm{pN}} - \beta_{\mathrm{p0}} = T_0 \left(\frac{\sigma_{\mathrm{p}}}{\sigma_0}\right)^{m_\sigma} N^{m_\alpha} \tag{30}$$

Where T_0, m_σ and m_α are dimensionless empirical factors.

2.6 Calibration of the macro-element modelling

The parameters in the HARM model that are needed to be calibrated can be classified in two categories: (a) parameters that define the shape of the backbone curve, (b) parameters that describe the ratcheting effect.

Abadie, (2015) proposed a methodology for calibration to identify each parameter based on continuous and long-term cyclic loadings tests. In addition, this calibration method is appropriate for models having similar behavior.

An empirical form of the backbone curve (Equation (31)) has been proposed by Abadie, (2015), is used for calibrating the model.

$$\varepsilon = \frac{\sigma}{E} + \varepsilon_{\mathrm{pu}} \left(\frac{\sigma}{k_{\mathrm{U}}}\right)^{m_h} \tag{31}$$

2.6.1 Backbone parameters calibration

The parameters that define the shape of the backbone curve are: the initial elastic young modulus E, the kinematic hardening parameters k_{n} and H_{n}, the ultimate strength k_{U}, the ultimate plastic strain $\varepsilon_{\mathrm{pu}}$ and the exponent m_{h} that defines the shape of the backbone.

- The initial elastic young modulus relates the stress and deformation for an isotropic elastic material. This linear law $\sigma/_E$ is performed only over the first few points of the initial loading curve where the behavior seems to be linear.
- The strengths of the sliders are increasing uniformly from the lower elastic limit (supposed to be equal to zero in Abadie et al., 2019) to the ultimate limit strength k_U. k_n therefore, can be expressed:

$$k_{\mathrm{n}} = k_{\mathrm{U}} \frac{n}{N_{\mathrm{s}}} \tag{32}$$

- The development of the hardening modulus is provided in the Appendix, and it leads to Equation (33).

$$\begin{cases} n = 1, & H_1 = \dfrac{k_{\mathrm{U}}}{\varepsilon_{\mathrm{pu}}} (N_{\mathrm{s}} - 1)^{m_{\mathrm{h}}-1} \\ 2 < n < N_{\mathrm{s}} - 1, & H_2 = H_1 \dfrac{(n-1)^{2-m_{\mathrm{h}}}}{m_{\mathrm{h}}(m_{\mathrm{h}}) - 1} \\ n = N_{\mathrm{s}}, & H_{N_{\mathrm{s}}} = 0 \end{cases} \tag{33}$$

- The ultimate strength was considered equal to the ultimate capacity. Both $\varepsilon_{\mathrm{pu}}$ and m_{h} should also fit the experimental data using Equation (31).

2.6.2 Ratcheting behavior

The ratcheting behavior is achieved using four parameters: initial ratcheting strain β_0, exponents m_r and m_s, and the initial ratcheting rate R_0.

- The initial ratcheting strain β_0 is considered as an arbitrary small value suggested equal to (1.0 x 10^{-4}) x ε_{pu} in Abadie et al., (2019).
- The exponent defining the decrease of ratcheting rate with cyclic history m_r is calibrated using Equation (34):

$$m_r = \frac{1}{m_\alpha} - 1 \tag{34}$$

- The exponent defining the increase of ratcheting rate with load intensity m_s is obtained using the Equation (35):

$$m_s = m_\sigma(m_r + 1) - m_h - 1 \tag{35}$$

- The initial ratcheting rate R_0 is obtained using Equation (36):

$$R_\beta = R_0\beta_0^{m_r} \tag{36}$$

2.7 Effect of cyclic loading on monotonic response

The influence of cyclic loading is explored first using experimental tests having the same load amplitude with increasing the number of cycles (Figure 14), and second using experimental tests by increasing the load magnitude (Figure 15). Both figures show that at the end of each unload-reload cycle, when exceeding the maximum cyclic loading, the reloading curve tends towards the backbone curve, which conforms to Masing rule.

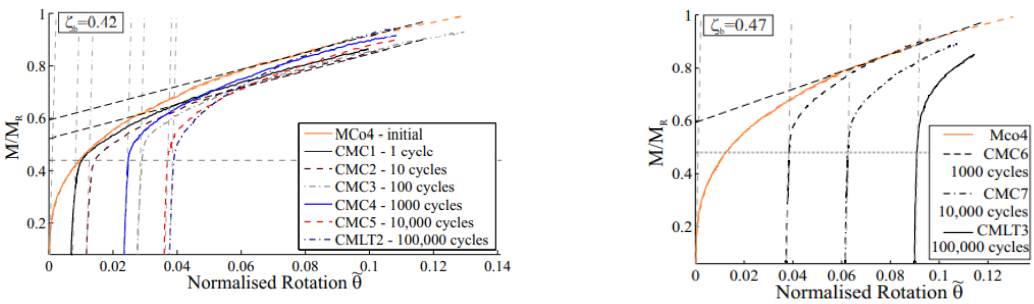

(a) (b)

Figure 14: Influence of cycle number on monotonic response: (a) Test series with (τ_b = 0.42) and (b) Test series with (τ_b = 0.47) (Abadie, 2015).

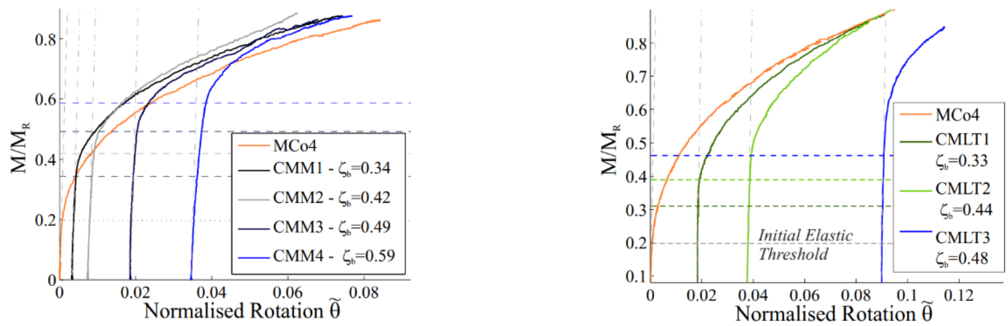

(a) (b)

Figure 15: Influence of maximum cyclic load magnitude on monotonic response: (a) 10 cycles test series (b) 100,000 cycles test series (Abadie, 2015).

3 Centrifuge modelling

3.1 General overview

In the field of geotechnical engineering, centrifuge modelling is a widely used tool since it allows studying the behavior of real structures on a small-scale model. The main purpose of spinning a $1/N_g$ scaled model in the centrifuge is to increase the centrifugal acceleration in the model to N_g times the earth's gravity in order to achieve the same stresses in the model as in the prototype. Thus, a scaling law (Garnier et al., 2007), was used to link the full scale to the small-scale model as listed in Table 1 : for instance, $x^* = x^{\text{model}}/x^{\text{prototype}}$.

Table 1: Scaling laws for different parameters (with $N_g = 100$)

Parameter	**Notation**	**Unit**	**Scaling factor**
Distance	$x*$	L	$1/Ng$
Stress	$\sigma*$	M/LT^2	1
Density	$\rho*$	M/L^3	1
Gravity	$g*$	L/T^2	Ng
Deformation	$\varepsilon*$	-	1
Velocity	$v*$	L/T	1
Acceleration	$a*$	L/T^2	Ng
Frequency	$f*$	1/T	Ng
Force	$F*$	ML/T^2	$1/N_g^2$

The Gustave Eiffel University's geotechnical centrifuge (formerly, IFSTTAR or LCPC) consists of a swinging basket attached through an arm to a central axis (Figure 16). This centrifuge has a maximum radius of 5.5 m from the axis to the platform of the basket, and its swinging basket permits the installation of a container with 1.40 m in length, 1.15 m in width and 1.50 m in height, and with embanked mass of 2000 kg for experiments at 100×g. More details about the centrifuge can be found in Thorel et al., (2009).

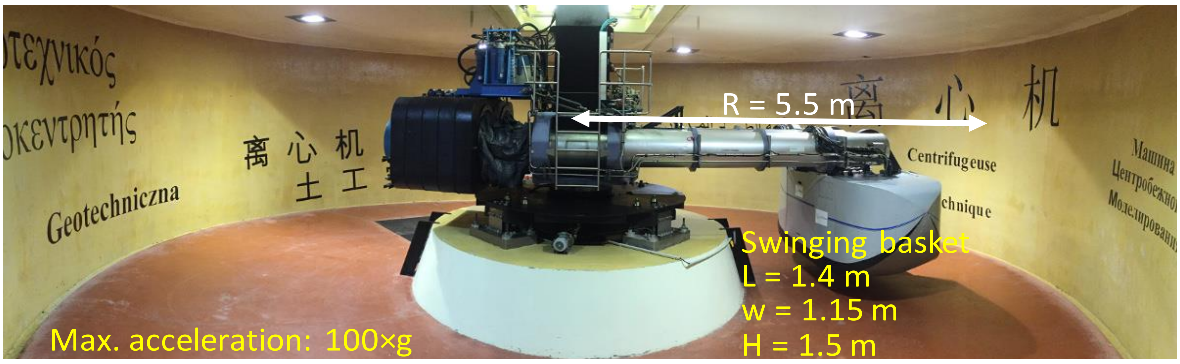

Figure 16: Gustave Eiffel University's geotechnical centrifuge.

All the tests are carried out on 1/100 scale monopile model at an acceleration level of $N_g = 100$ times the earth's gravity.

3.2 Monopile model

The monopile model is a 525 mm (length) by 50 mm (outside diameter) by 2.5 mm (thickness) open-ended circular aluminium 2017A tube. The geometric and mechanical characteristics of the monopile in model and prototype scale are described in Table 2.

Table 2: Geometric and mechanical characteristics of the monopile.

Parameter	Model	Prototype
D (m)	0.05	5
E (GPa)	72.5	72.5
G (GPa)	27.2	27.2
l (m)	0.525	5.25
L (m)	0.25	25
t (m)	0.0025	0.25

3.3 Soil model

The soil model is a poorly graded NE34 Fontainebleau sand (Table 3) with a relative density of 82% obtained by air pluviation into a rectangular strongbox of internal dimensions 1200 mm × 800 mm × 360 mm (length × width × height). To simulate the prototype condition where the foundation is under water, the specimen is then saturated by injecting tap water through four draining channels located at the bottom of the strongbox (Figure 17 (a)). The effective unit weight of the saturated sand is 10.26 kN/m^3.

Table 3: Characteristics of Fontainebleau NE34 sand (Klinkvort RT, 2018).

Sand	d_{50} (μm)	ρ_s (g/cm^3)	ρ_{dmin} (g/cm^3)	ρ_{dmax} (g/cm^3)
Fontainebleau NE34	210	2.65	1.434	1.746

3.4 Experimental set-up

A special device is developed to install the monopile in flight at 100×g and then apply horizontal loading without stopping the centrifuge to maintain the states of stress that have been induced by the installation of the monopile beforehand. The set-up (Figure 17) had two main axes. (i) Vertically, a miniature electro-mechanical hammer was controlled by a hydraulic actuator to drive the monopile to the desired embedment depth of 250 mm. (ii) Horizontally, an electro-mechanical actuator is activated to laterally load the head of the monopile from an eccentricity l_e = 250 mm (i.e. 5D) from the ground level. Maatouk et al., (2021) have given a more detailed description of the experimental set-up and test procedure.

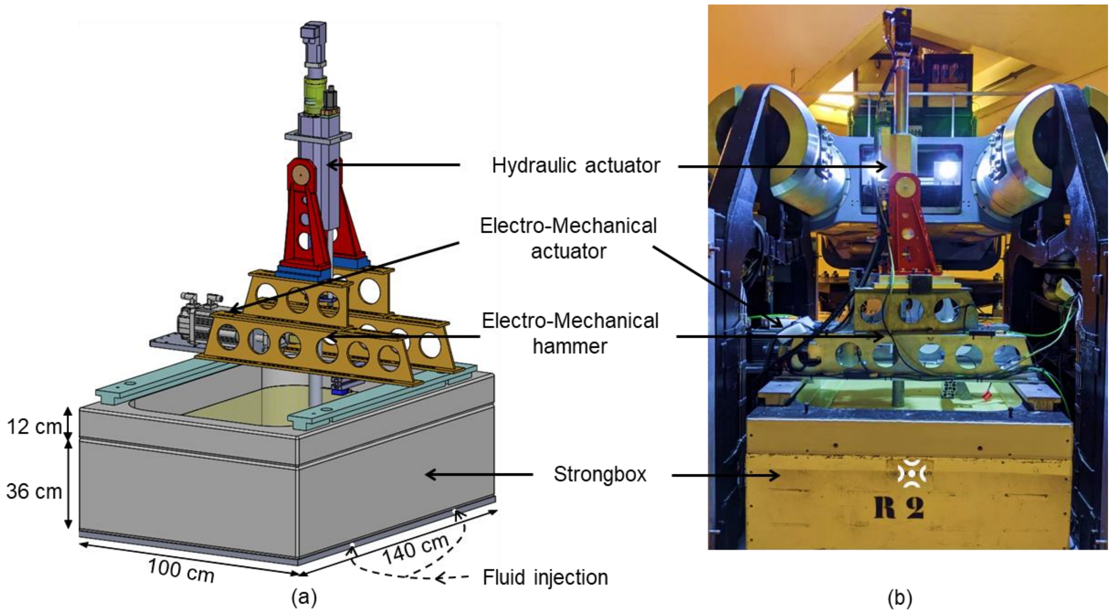

Figure 17: Experimental set-up: (a) Schematic drawing, (b) in the centrifuge basket

3.5 Experimental campaign

Three tests are conducted in the same strongbox on a monopile installed by impact-driven at 100×g. However, the horizontal loads (*H*) are applied with different manner. A monotonic horizontal test is carried out with a constant speed of 0.1 mm/s by pushing the monopile horizontally 50 mm from its head. The remaining tests are performed cyclically with different amplitudes and similar number of cycles of 5000 and frequency of 0.4 Hz. Table 4 lists the experimental campaign that is realized in this study

Table 4: Experimental campaign in model scale

Test	Nomenclature	H_{max} (daN)	H_{min} (daN)	Comments
Monotonic load	M	-	-	-
Cyclic load with **M**edium amplitude	CM	95	0	Cyclic load starts for a $\theta_G = 0.35°$
Cyclic load with **H**igh amplitude	CH	141	4.5	Cyclic load starts for a $\theta_G = 0.57°$

4 Numerical model and results

The modelling method for the analysis of monopile foundations subjected to cyclic loadings, used in this research, is based on a 0-D macro-element model using the HARM constitutive approach detailed in the literature. The limitations of this model is that the local soil behavior down the monopile can not be captured so that solely the global monopile response at the load application H-ν_T, is identified.

The monopile global response in the stress-strain space is obtained with the normalization of the lateral force H and the monopile top displacement ν_T with the corresponding reference values as mentioned in Section 2.5.1. They are determined based on the ultimate capacity of the monopile corresponding to a displacement at ground level of $\nu_G = 0.1D$, where D is the diameter of the monopile. From the monotonic test 'M', the response is carried out on a prototype monopile of diameter $D = 5$ m embedded over $5D$ into water-saturated dense sand with an eccentricity $l_e = 5D$, the reference values are $H_R = 26.51$ MN and $\nu_{TR} = 1.6$ m.

4.1 Backbone curve results

4.1.1 Pure kinematic hardening

The analytical response of the initial loading curve, for the first case where the ratcheting is not considered ($R_\beta = 0$), is determined using the incremental plastic strain as described in Equation (24). The sum of the accumulated plastic strains governed by each yield surface leads to the total monopile response.

Four model parameters are needed to define the shape of the backbone curve: elastic modulus E, ultimate plastic strain ε_{pu}, ultimate stress k_U, and the exponent m_h. The analytical values of these parameters can be found using the calibration method of the backbone as previously described in Section 2.6.1. The resultant backbone curve is then compared to the experimental response obtained from the monotonic test (M) in prototype scale.

The numerical algorithm, specified below, is performed using iteration steps described as follow: the stress applied on the top of the monopile, is considered as an increasing stress vector σ ranging from 0 to the maximum ultimate stress σ_p. When a value of the stress vector is found higher than the ultimate strength of any yield surface, then a new surface will get into action while producing an additional plastic strain.

Input: E, k_U, ε_{pu}, N_s, k_n, H_n

Determination of k_n, H_n with $n = 1, \dots, N_s$

$\sigma \leftarrow [0{:}\sigma_p]$

for $i = 1 \dots N_S$

  if $\sigma_i > k_i$ then

    $\alpha_i = \frac{\sigma_i - k_i}{H_i}$

  else $\alpha_i = {}^{\sigma_i}/_{E}$

  end if

end for

Output: σ_i, α_i

The numerical model parameters for the calibration of the experimental tests are: $E_0 = 2.25$; $k_{\mathrm{U}} = 1.5$; $\varepsilon_{\mathrm{pU}} = 1.5$ and $m_{\mathrm{h}} = 3.5$.

The application of the above algorithm leads to Figure 18 where a good correlation is shown between the predicted HARM model with ratcheting disabled and the monopile response obtained from the monotonic test (M).

Besides, the empirical power law described in Equation (31), with the same four parameters used in the HARM model, is also verified and it showed a good fit with the experimental results (Figure 19).

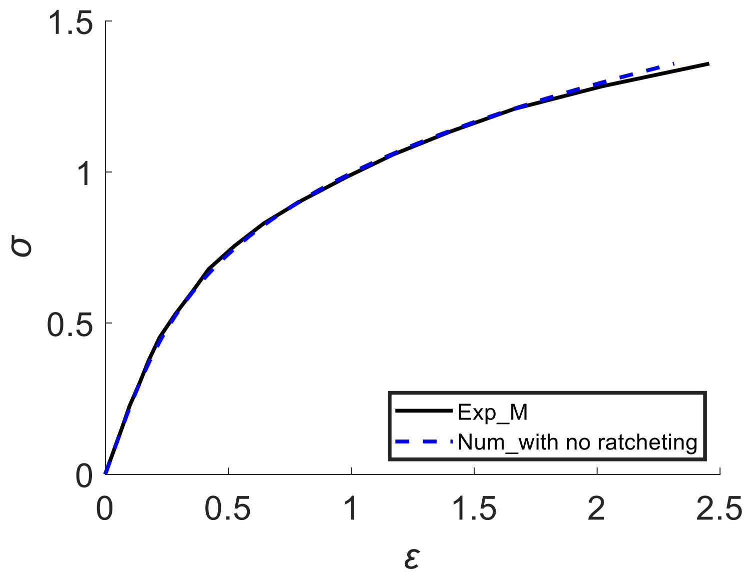

Figure 18: Compared experimental data with the HARM prediction ($R_\beta = 0$, $m_h = 3.5$) for test (M).

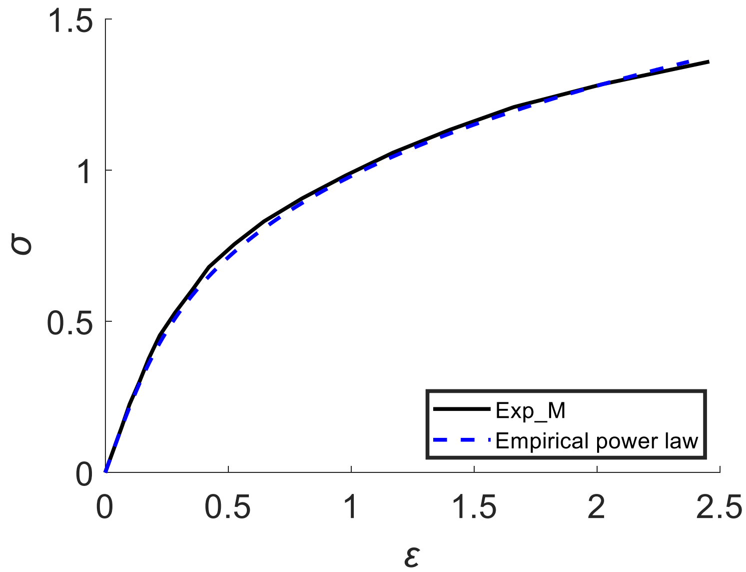

Figure 19: Compared experimental data with the empirical power law ($m_h = 3.5$) for test (M).

4.1.2 Effect of ratcheting on backbone curve

The total monopile response is achieved by adding the ratcheting strain of the initial loading curve described in Equation (25) to the pure kinematic plastic strain described in Equation (24).

Other four input parameters are therefore needed to capture the total response: initial ratcheting strain β_0, initial ratcheting rate R_0, exponents m_r and m_s characterizing respectively the dependence of the ratcheting rate on the hardening parameter and on the stress level.

Adding ratcheting to the backbone curve, decreases the resistance with respect to the pure kinematic hardening curve. The total monopile response (red dotted curve in Figure 20), therefore, falls down below the experimental backbone curve. So that, an additional calibration must be performed to improve the resistance of the curve in order to fit the experimental results again. This calibration is achieved by optimizing the values of the hardening modulus H_n (calibration of the exponent m_h). Thus, the resultant green dotted monopile response after correction is obtained as shown in Figure 20. The analytical and optimized calibrated parameters are summarized in Table 5.

Table 5: Parameter values for the calibration of the HARM model.

Backbone curve (pure kinematic hardening)	Analytical	Optimized
E_0	2.25	2.25
k_U	1.5	1.5
ε_pu	1.5	1.5
m_h	3.5	5
Ratcheting behavior		
β_0	1.5×10^{-4}	1.5×10^{-4}
m_α	0.21	0.15
m_σ	3	2.8
R_beta	0.8	0.8

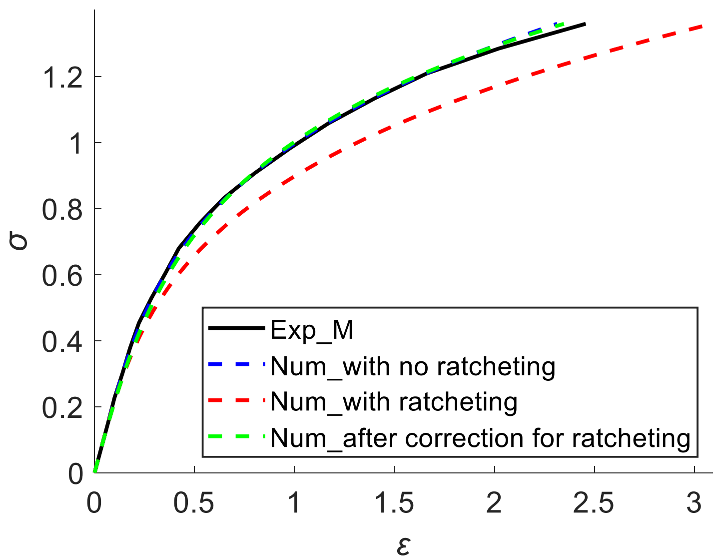

Figure 20: Prediction of the backbone curve (test) without ratcheting, with ratcheting with and without optimization correction of the H_n.

4.2 Subsequent cyclic loading results

The monopile cyclic response is obtained following the procedure for the unloading-reloading curves as described in Section 2.5.3.3, and compared to cyclic response of the medium and the high amplitude tests (CM and CH respectively). The maximum and minimum stresses of both tests shown in Table 6 are deduced from $H_{\max}$ and $H_{\min}$ of Table 4. The values of $\sigma_{\max}$ and $\sigma_{\min}$ are needed in the numerical code.

Table 6: Maximum and minimum stresses for medium and high amplitude tests.

Test	**Nomenclature**	$\sigma_{\max} = \frac{H_{\max}}{H_{\mathrm{r}}}$	$\sigma_{\min} = \frac{H_{\min}}{H_{\mathrm{r}}}$
Cyclic load with Medium amplitude	CM	0.36	0
Cyclic load with High amplitude	CH	0.53	0.017

The cyclic response is presented as straight lines between the maximum and minimum cyclic points for each cycle, and it is performed for a few number of cycles $N = [1\ 2\ 5\ 10\ 20\ 50\ 100\ 200\ 500\ 1000\ 2000\ 5000]$.

The results show a better fit for the medium amplitude (Figure 22) more than the high amplitude (Figure 21).

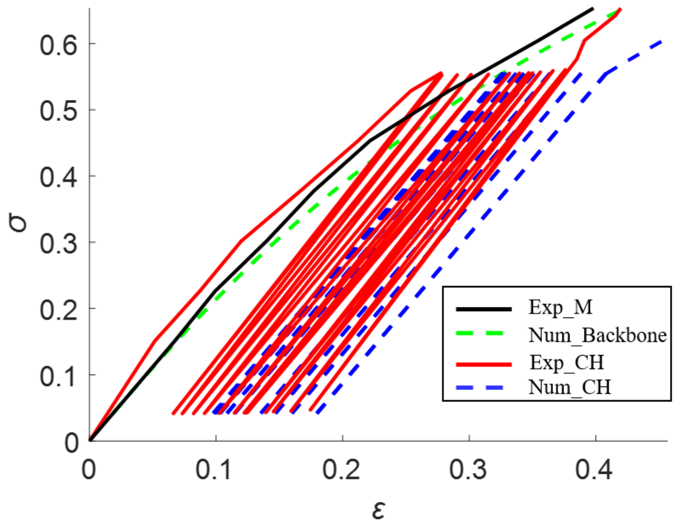

Figure 21: High amplitude test vs HARM prediction.

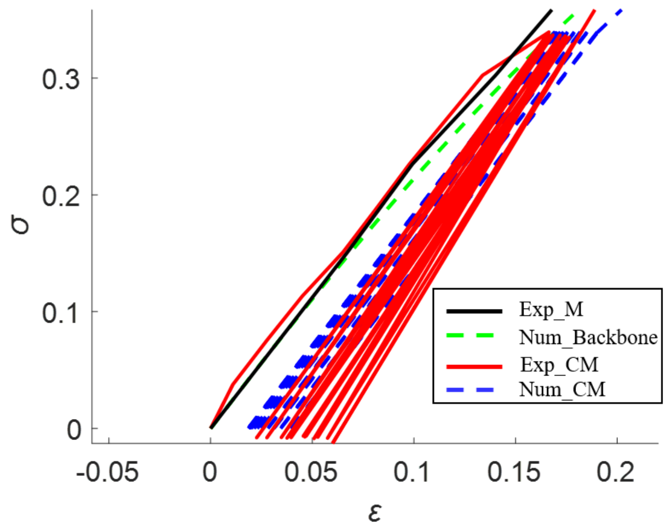

Figure 22: Medium amplitude test vs HARM prediction.

4.3 Residual deformation at minimum peak load

The experimental and numerical total deformation at the minimum cyclic load are plotted, in Figure 23, against the number of cycles for both tests. The numerical results are achieved from the power law (Equation (30)) for the same vector of cycle number of the previous section.

The results may show a better fit if a logarithmic law is used instead of a power law, because a logarithm law makes the curve more linear.

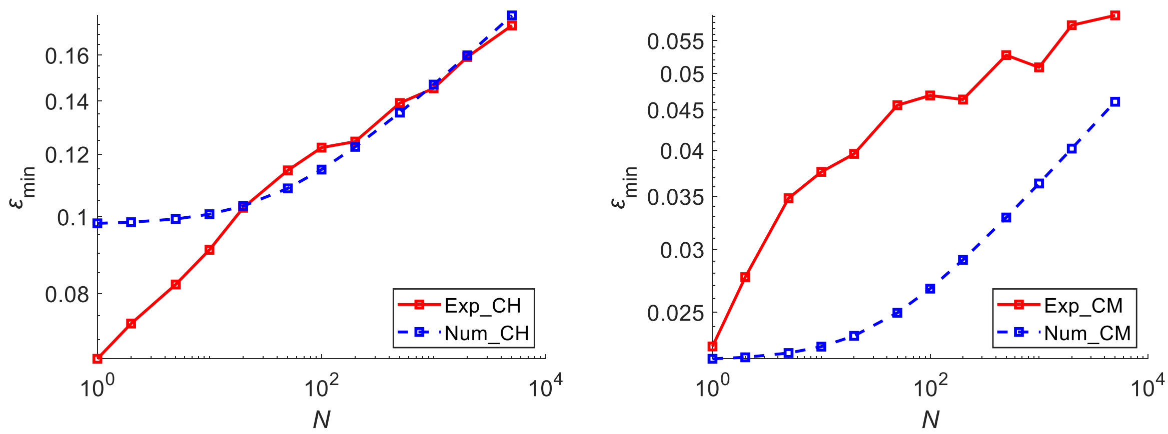

(a) (b)

Figure 23: Prediction of the residual deformation at minimum peak load (a) high amplitude test and (b) medium amplitude test

4.4 Post-cyclic results

The influence of cyclic loading on the monotonic response is explored using the post-cyclic curve which is plotted from the final unloading at minimum peak load for both high amplitude and medium amplitude testing as illustrated in Figure 24 and Figure 25 respectively.

As observed for the predicted curves (dotted blue), when exceeding the maximum cyclic loading, the reloading curve is always down the backbone curve (Masing rule). In contrast, due to experimental errors, this feature is not observed experimentally.

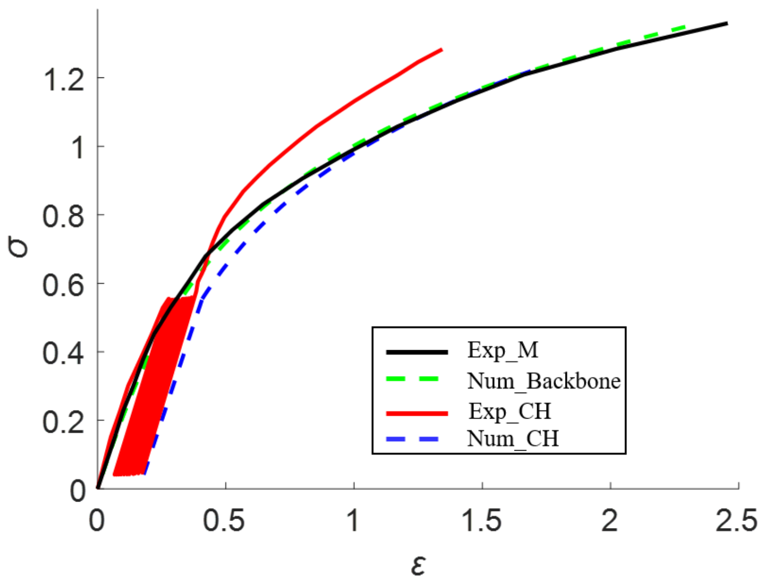

Figure 24: Post-cyclic for the high amplitude cycle

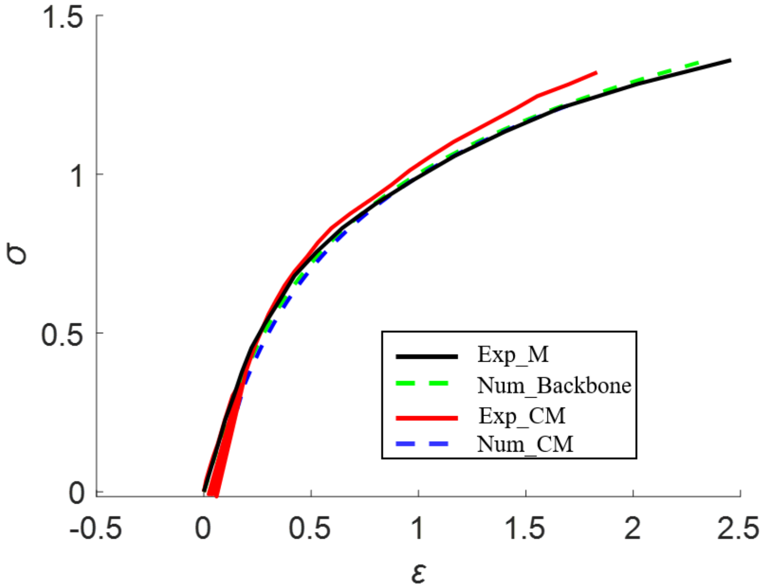

Figure 25: Post-cyclic for the medium amplitude cycle

5 Conclusions

This research outlines a constitutive model that predicts the response of rigid monopiles when subjected to cyclic lateral loading in cohesionless soil for offshore wind applications. The monopile response obtained from the numerical model are then compared with that resultant from experiments conducted in centrifuge at 100xg.

The numerical approach used is based on a macro-element model. It is a simplified model that detects the response at the head of the monopile and the monopile-soil interaction is represented by springs at the ground-level of the foundation. The constitutive modelling of ratcheting (HARM model) is bordered within the hyperplasticity framework described by Houlsby and Puzrin, (2006) based on thermodynamic laws. The model uses multiple kinematic surfaces to produce a smoother response, and generates an additional plastic strain governed by the ratcheting element. A particular feature of the HARM model is that it conforms to Masing rule.

The experimental work presented in this research involves a monotonic test and two cyclic tests for calibrating the backbone curve and the hysteretic loops respectively. The experimental campaign is conducted using a special set-up on a centrifuged monopile model impact-driven into a saturated dense sand.

The numerical model captures approximately the behavior observed experimentally using the calibration method proposed by Abadie, (2015). An accurate fit of the experimental results may be obtained by using a logarithmic law for the formulation of the accumulation of ratcheting strain instead of a power law.

6 Recommendations for future work

According to the findings in this research, future suggestions may be proposed to more understand the monopile response under cyclic loading:

- This research studies the monopile response under a single amplitude cyclic loading. It should be interesting to evaluate the monopile behavior after performing a Multi-amplitude cyclic loading and implementing a load history. Like that, one may check the Masing behavior, the ratcheting effect and the hysteresis loop shape.
- The present study compare the monopile response under cyclic loading obtained from experiments with the numerical HARM model. Very high cyclic loading (storm loads) is necessary to be conducted to ensure if the experiments are also representative for the HARM prediction.
- Other macro-element models may be used in order to see which numerical model fit well the centrifuged experimental tests (Wichtmann and Triantafyllidis, 2017).

7 References

Abadie CN, Houlsby GT and Byrne BW (2019) A method for calibration of the Hyperplastic Accelerated Ratcheting Model (HARM). *Computers and Geotechnics*, vol. 112, pp. 370–385. https://doi.org/10.1016/j.compgeo.2019.04.017

Abadie CN (2015) *Cyclic Lateral Loading of Monopile Foundations in Cohesionless Soils*. Doctoral Dissertation, University of Oxford. http://www.eng.ox.ac.uk/civil/publications/theses/abadie

Achmus M, Kuo YS and Abdel-Rahman K (2009) Behavior of monopile foundations under cyclic lateral load. *Computers and Geotechnics*, **36(5):** 725–735. https://doi.org/10.1016/j.compgeo.2008.12.003

Beuckelaers WJAP, Houlsby GT and Burd HJ (2018) A Comparison of the Series and Parallel Masing-Iwan Model in 2D. In *Numerical Methods in Geotechnical Engineering IX*, pp. 173–178.

Beuckelaers WJAP (2017) *Numerical Modelling of Laterally Loaded Piles for Offshore Wind Turbines*. Doctoral dissertation, University of Oxford.

Byrne BW, McAdam RA, Burd HJ et al., (2017) PISA: New design methods for offshore wind turbine monopiles. In *Offshore Site Investigation Geotechnics (OSIG)-Smarter solutions for Future Offshore Developments: Proceedings of the 8th International Conference.* Society for Underwater Technology, London, UK, vol. 1, pp. 142–161. https://doi.org/10.3723/osig17.142

Byrne BW, Byron W, Houlsby GT et al., (2020) PISA: Design model for monopiles for offshore wind turbines: Application to a stiff glacial clay till. *Geotechnique*, **70(11):** 1030–1047. https://doi.org/10.1680/jgeot.18.P.255

Byrne BW, Byron W and College M (2000) *Investigations of Suction Caissons in Dense Sand*.

Dupla JC, Palix E, Damblans G et al., (2019) Le projet ANR SOLCYP+ pour améliorer le dimensionnement des monopieux utilisés comme fondations d'éoliennes marines. *Revue Française de Géotechnique*, 158. https://doi.org/10.1051/geotech/2019010

Winkler E (1867) *Die Lehre von der Elasticität und Festigkeit*, 1st edition, H. Dominicus, Prague.

Ziegler H (1977) *An introduction to thermomechanics*, 1st edition, North Holland, Amesterdam.

Houlsby GT, Abadie C N, Beuckelaers WJAP and Byrne BW (2017) A model for nonlinear hysteretic and ratcheting behaviour. *International Journal of Solids and Structures*, vol. 120, pp. 67–80. https://doi.org/10.1016/j.ijsolstr.2017.04.031

Houlsby GT, Cassidy MJ and EinavI (2005) A generalised Winkler model for the behaviour of shallow foundations. *Geotechnique*, **55(6):** 449–460. https://doi.org/10.1680/geot.2005.55.6.449

Houlsby GT and Puzrin AM (2006) Thermodynamics of Porous Continua. In *Modern trends in geomechanics*, Springer, Berlin, Heidelberg, pp. 39–60. https://doi.org/10.1007/978-3-540-35724-7_3

Klinkvort RT (2018) *Centrifuge monopile tests in sand. Factual report of laboratory testing. NGI Technical note*.

Maatouk S, Blanc M and Thorel L (2021) Impact driving of monopiles in centrifuge: effect on the lateral response in sand. *International Journal of Physical Modelling in Geotechnics*, pp. 1–33. https://doi.org/10.1680/jphmg.21.00035

Masing. (1926) *Eiganspannungen and verfestigung beim messing*, pp. 332–335.

Prager W (1955) The Theory of Plasticity: A Survey of Recent Achievements. In *Proceedings of the Institution of Mechanical Engineers*, London, **169(1):** 41–57. https://doi.org/10.1243/pime_proc_1955_169_015_02

Puzrin AM and Houlsby GT (2001) Fundamentals of kinematic hardening hyperplasticity. *International Journal of Solids and Structures*, **38(21):** 3771–3794. https://doi.org/10.1016/S0020-7683(00)00238-9

Schroeder FC et al., (2015) Predicting monopile behaviour for the godewind offshore wind farm. *Frontiers in Offshore Geotechnics III* - In *Proceedings of the 3rd International Symposium on Frontiers in Offshore Geotechnics, ISFOG 2015*, pp. 735–740. https://doi.org/10.1201/b18442-101

Sørensen SPH et al., (2017) Consequences of p-y curve selection for monopile design for offshore wind turbines. In *Proceedings of the 8th International Conference on Offshore Site Investigation and Geotechnics*, London, pp. 1062-1069.

Staubach P and Wichtmann T (2020) Long-term deformations of monopile foundations for offshore wind turbines studied with a high-cycle accumulation model. *Computers and Geotechnics*, vol.124. https://doi.org/10.1016/j.compgeo.2020.103553

Thorel L et al., (2009) Mesures en macrogravité sur modèles réduits d ’ ouvrages géotechniques.

Wichtmann T and Triantafyllidis T (2017) Strain accumulation due to packages of cycles with varying amplitude and/or average stress – On the bundling of cycles and the loss of the cyclic preloading memory. *Soil Dynamics and Earthquake Engineering*, vol.101, pp. 250–263. https://doi.org/10.1016/j.soildyn.2017.07.012

WindEurope (2021) Offshore wind in Europe - Key trends and statistics 2020. *WindEurope*, **3(2):** 14–17.

Appendix

Derivation of the hardening modulus

From Figure 7(a), the tangent modulus can be expressed as:

$$\begin{cases} n = 1, & \dfrac{1}{E_{t1}} = \dfrac{\varepsilon(k_2) - \varepsilon(k_1)}{k_2 - k_1} \\ 1 < n < N_S, & \dfrac{1}{E_{tn}} = \dfrac{\varepsilon(k_{n+1}) - \varepsilon(k_n)}{k_{n+1} - k_n} \\ n = N_S, & E_{tN_S} = 0 \end{cases} \tag{37}$$

In another terms, using Equation (8), the tangent modulus can be formulated:

$$\begin{cases} n = 1, & \dfrac{1}{E_{t1}} = \dfrac{1}{E} + \dfrac{1}{H_1} \\ 2 < n < N_S - 1, & \dfrac{1}{E_{tn}} = \dfrac{1}{E_{tn-1}} + \dfrac{1}{H_n} \\ n = N_S, & E_{tN_S} = 0 \end{cases} \tag{38}$$

The hardening modulus can therefore be obtained by combining the previous equations with Equation (31) and Equation (32):

$$\begin{cases} n = 1, & H_1 = \dfrac{k_U}{\varepsilon_{pu}} (N_S - 1)^{m_h - 1} \\ 2 < n < N_S - 1, & H_2 = H_1 \dfrac{(n-1)^{2-m_h}}{m_h(m_h - 1)} \\ n = N_S, & H_{N_S} = 0 \end{cases} \tag{39}$$